ELSEVIER

Journal of Structural Geology 27 (2005) 571–585

JOURNAL OF STRUCTURAL GEOLOGY

www.elsevier.com/locate/jsg

Mantled porphyroclast gauges

Daniel W. Schmid[a,*], Yuri Yu. Podladchikov[b]

[a]*Geologisches Institut, ETH Zentrum, Zürich, Switzerland*
[b]*Physics of Geological Processes, University of Oslo, Pb 1048 Blindern, 0316 Oslo, Norway*

Received 18 September 2002; received in revised form 1 July 2004; accepted 20 September 2004
Available online 25 January 2005

Abstract

We investigate the behavior of the isolated mantled porphyroclast in a shear zone. The method employed is a finite element model. Three distinct phases, clast, mantle and matrix are present, the rheologies are power-law with exponents ranging from 1 to 5 and the far-field boundary condition is simple shear. The effective viscosity of the mantle is assumed to be less than those of the clast and the matrix. We show for which parameter sets mantled porphyroclasts reach super-horizontal stabilization with respect to the shear plane and sense. Clasts in natural mylonites frequently exhibit similar orientations, which are interpreted as stable inclinations. The systematic examination of the matrix–mantle–clast system allows for the construction of attractor maps that can be directly used as gauges for (i) the effective viscosity contrast between matrix and mantle, (ii) the production rate of mantle material around the clast as a function of the bulk shear strain, and (iii) for the total shear strain. The necessary data required to use the attractor maps are simple geometrical parameters that can be measured in the field, i.e. clast aspect ratio, clast inclination versus the shear plane, mantle thickness, and mantle and clast area. This new method successfully reproduces the characteristics of natural porphyroclasts and is in good agreement with data from natural shear zones.

Keywords: Rotating clasts; Stabilization; Back-rotation; Lubrication; Numerical modeling; Rheology; Shear strain estimation

1. Introduction

The frequent observation of mantled porphyroclasts in mylonitic shear zones in combination with their distinct geometries and often systematic orientation has stimulated a major quest to find possible applications as gauges capable of providing quantitative data on rheology, kinematics, and dynamics. While there appears to be common agreement on the usefulness of mantled porphyroclasts as indicators of shear sense (e.g. Hanmer and Passchier, 1991), all other possible interpretations as natural microgauges are still disputed. In particular, it is unclear if and how mantled porphyroclasts record information on the vorticity of the bulk flow (Ghosh and Ramberg, 1976; Marques and Coelho, 2001; Pennacchioni et al., 2001; ten Grotenhuis et al., 2002; Mancktelow et al., 2002; Ceriani et al., 2003; Schmid and Podladchikov, 2004; Taborda et al., 2004), if they are reliable measures of rheology (Passchier et al., 1993; Bons et al., 1997; Pennacchioni et al., 2000; Piazolo et al., 2002), and to which extent they record finite strain (e.g. Piazolo and Passchier, 2002).

We believe that much of the uncertainty stems from the fact that the most basic requirement to study mantled porphyroclasts in a shear zone is often disregarded, namely that the mantled porphyroclasts in a matrix represents a three-phase system: the clast, the mantle, and the matrix. Consequently three possibly different material properties must be introduced. Nevertheless, previous studies have frequently modeled the mantle as a passive strain tracker in the matrix, starting from Passchier and Simpson's (1986) pioneering work. Furthermore, the clast is often designated rigid, essentially reducing the three-phase system to one single rheological phase.

This single-phase reduction is also inherent to the usually employed ellipse-shape based analytical solutions. The

* Corresponding author. Present address: Physics of Geological Processes, University of Oslo, Pb 1048 Blindern, 0316 Oslo, Norway. Tel.: +47-2285-6484; fax: +47-2285-5101
E-mail address: schmid@fys.uio.no (D.W. Schmid).

0191-8141/$ - see front matter © 2005 Elsevier Ltd. All rights reserved.
doi:10.1016/j.jsg.2004.09.005

well-known solution for rigid particles in simple shear was derived by Jeffery (1922) and extended to contemporaneous pure and simple shear by Ghosh and Ramberg (1976). The interest in the behavior of isolated inclusions is, however, not restricted to geology but is relevant to a large part of the scientific community. Based on the alternative analytical solutions by Muskhelishvili (1953) and Eshelby (1959), researchers in the fields of composites and defects in solids have derived expressions for inclusions with imperfect bonding to the matrix (e.g. Mura, 1987; Furuhashi et al., 1992; Gao, 1995; Ru and Schiavone, 1997; Shen et al., 2001). An important finding of these recent works is that the so-called Eshelby conjecture (Mura, 2000) does not hold for a cylindrical or elliptical inclusion with a slipping interface. The Eshelby conjecture states that homogeneous, i.e. constant with respect to spatial coordinates, stresses applied at infinity cause constant stresses inside the inclusion. Irrespective of inclusion orientation, aspect ratio, and actual combination of pure and simple shear, the stress state inside the inclusion can be completely described by a single tensor. This result is of fundamental significance for geological applications, where the observed systems are likely to show imperfect bonding between clast and matrix; either due to interfacial slip or the presence of a third (mantle) phase. Inhomogeneous stress states inside the inclusion are not only expected to change the flow patterns, but may cause transitions into different deformation mechanism fields, drive metamorphic reactions, and be the cause for asymmetric zoning (e.g. myrmekite distribution; Simpson and Wintsch, 1989).

The subject of this paper is the two-dimensional, numerical modeling study of the isolated three-phase (mantled) porphyroclast system with elliptical geometries, subject to simple shear. Given the large natural differences in grain sizes between clast and mantle material and the amount of strain localization in the mantle we assume that the mantle material is the weakest (lowest effective viscosity) phase in the system and analyze the consequences of this hypothesis. In the context of the numerical models we will refer to this weak mantle material as 'lubricant', which is a geologically neutral terminology, also applicable to the end-member case where the thickness of the lubricant vanishes, but slip is allowed on the inclusion–matrix interface (e.g. Samanta and Bhattacharyya, 2003).

In the following section of the paper the model method and setup are explained. Then the influence of a lubricating layer on the stress distribution and the rotation rate at initial and finite stages is demonstrated with examples of circular and elliptical inclusions. Finally we show under which conditions lubricated inclusions have stable positions and how viscosity contrast between matrix and lubricant, the production rate of fine-grained mantle material, and the accumulated bulk shear strain can be estimated from geometrical parameters by means of attractor maps.

2. Numerical method and setup

The numerical model used is a personally developed (by the first author) two-dimensional FEM code using the seven node Crouzeix–Raviart triangle (Crouzeix and Raviart, 1973) to solve the Stokes equations for incompressible, slowly creeping, viscous materials. A mixed method is employed, with linear interpolation of pressure, which avoids spurious pressures usually appearing due to the incompressibility constraint (Brezzi and Fortin, 1991).

The initial configuration of the numerical experiments is depicted in Fig. 1. Since the presence of boundaries may influence the behavior of a rotating inclusion (Ildefonse et al., 1992; Bons et al., 1997; Marques and Coelho, 2001), care was taken to avoid such boundary effects. In all models, the length of the clast is only 5% of the shear zone width and the lateral boundaries are even farther apart, with the length of the ellipse only 1–2% of the box length. The thickness of the lubricating layer, H, is given in percent of the local ellipse radius and ranges from 0 to 50%. The boundary conditions applied to all sides of the experimental box are (constant shear strain rate) simple shear velocities. The definition of the shear strain rate is:

$$\dot{\gamma} = \frac{\partial v_x}{\partial y} \tag{1}$$

where v_x is the horizontal velocity in the Cartesian coordinate system (Fig. 1). Hence positive $\dot{\gamma}$ values denote top to the right shearing, which is the case for all presented experiments.

The studied rheologies are Newtonian and non-Newtonian power-law, for which the relationship between deviatoric stresses, τ_{ij}, and strain rates, $\dot{\varepsilon}_{ij}$, can be written

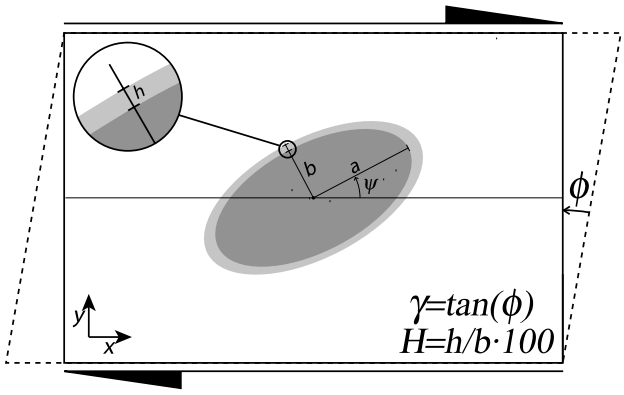

Fig. 1. Initial experiment configuration. A highly viscous ellipse (dark gray) is coated with a low viscous, lubricant layer (light gray), and embedded in a matrix of intermediate effective viscosity. The sketch is not to scale with respect to the actual clast–matrix size relationship. The aspect ratio of the ellipse is given by the ratio of the two axes, a/b. The orientation of the inclusion is measured as the angle ψ, between the long axis and the shear plane, with $\psi > 0$ designating counterclockwise values. The thickness of the lubricant, H, is measured in percent of the local ellipse radius. The boundary conditions applied are simple shear velocity on all sides. The shear angle ϕ is a measure of the achieved shear strain γ.

in general form as (e.g. Ranalli, 1995):

$$\tau_{ij} = 2\eta\dot{\varepsilon}_{ij} \tag{2}$$

η is the effective viscosity of the material and defined as:

$$\eta = B\dot{\varepsilon}_{\mathrm{e}}^{(1/n-1)} \tag{3}$$

where $\dot{\varepsilon}_{\mathrm{e}}$ is the effective strain rate, n is the power-law exponent, and B is a pre-exponential material constant, which in the case of a Newtonian material ($n=1$) is the viscosity. The definition of $\dot{\varepsilon}_{\mathrm{e}}$ is:

$$\dot{\varepsilon}_{\mathrm{e}} = \sqrt{\left(\frac{\dot{\varepsilon}_{xx} - \dot{\varepsilon}_{yy}}{2}\right)^2 + \dot{\varepsilon}_{xy}^2} \tag{4}$$

and follows the Mohr circle construction (Jaeger and Cook, 1979) of the maximum or effective shear stress σ_{e}:

$$\sigma_{\mathrm{e}} = \sqrt{\left(\frac{\tau_{xx} - \tau_{yy}}{2}\right)^2 + \tau_{xy}^2} \tag{5}$$

For scalability the viscosities are given as relative values. Unless stated otherwise, the clast is assumed to be 1000 times stronger, i.e. more viscous, than the matrix. The viscosity of the lubricant is a fraction of the matrix viscosity ranging from 1:2 to 1:50,000. While viscosity contrasts are clearly defined for Newtonian materials, the case of power-law materials is less straightforward, because a priori unknown strain rates enter the expression of the effective viscosities. As a proxy, the applied far-field strain rate values may be used to evaluate the effective viscosities. However, due to the expected strain rate localization in the weak lubricant, the calculated values will not correspond to the actual experiment values. Ten and Yuen (1999) have pointed out that even a small difference in the values of clast and matrix behaving as power-law materials can result in large effective viscosity contrasts.

Concerning the finite element mesh resolution the following strategy was used. (1) The sharpest gradients in material properties and resolution occur in and near the clast–lubricant couple. Therefore the required mesh resolution is here highest. Further away, in the matrix, the material properties are constant and the solution parameters close to the far-field boundary condition values, which is easily resolved with a rather coarse mesh. Typical total mesh resolutions are 50,000 elements and 200,000 nodes. (2) Due to the large overall and local strains expected for the problem, continuous remeshing was applied for the finite strain runs, whereby the surrounding box was kept rectangular and only the contours of the lubricant layer and the elliptical inclusion were actually moved and a new mesh was generated for every time step. With this procedure, the danger of mesh distortion is eliminated and the only restriction on achievable strains results from the increasing memory usage due to the ever-growing number of elements, caused by the formation of tails and thinning of the lubricant around the ellipse.

3. Circular inclusions

3.1. Initial stages—Newtonian

In order to understand the characteristics of lubricated clasts we start with the simplest one, having a circular shape and Newtonian rheologies. A series of six different experiments are analyzed in terms of pressure p (Fig. 2) and the corresponding maximum shear stress values (Fig. 3). Note that compressive pressures are positive and only perturbation values are shown. Hence an arbitrary lithostatic component may be added without any influence on the results. Furthermore, all stress components are normalized by the characteristic far field stress, i.e. $\dot{\gamma}\eta_{\mathrm{matrix}}$.

The end-member cases of clasts are the very strong (Fig. 2a) and the very weak (Fig. 2d), with no lubricant layer present. As expected, high pressures occur adjacent to the strong inclusion in the two quadrants where the simple shear streamlines impinge on the inclusion. The other two quadrants are in relative tension, exhibiting pressure lows that would in nature be the potential sites for the development of pressure shadows (e.g. Passchier and Trouw, 1996). Due to the symmetry of the system, the absolute amplitudes of the pressure perturbations in all four quadrants are equal. If the viscosity contrast between clast and matrix is flipped from 1000:1 to 1:1000 (Fig. 2d), not only the viscosity contrast is inverted but also the pressure perturbation field: compressional areas become tensional and vice versa. Interestingly the inside of the inclusion remains at background (lithostatic) pressure in the case of a strong as well as a weak clast.

Similar observations can be made in the case of the maximum shear stress, which also undergoes a ‘flip’ if the viscosity contrast is inverted (Fig. 3a and d). In contrast to the pressure, the maximum shear stress values inside the clast are sensitive to the viscosity contrast between clast and matrix. If the clast is strong it must resist the applied far-field flow conditions and therefore σ_{e} is high; if the clast is weak, it readily deforms with the applied simple shear and therefore the stresses are low. In order to map between stress and strain rate, the displayed maximum shear stress must be divided by two times the material viscosity to obtain the maximum shear strain rate, cf. Eqs. (2), (4) and (5). An example of this mapping is given with the effective strain rate insert in Fig. 3f.

The introduction of a lubricant layer between the strong clast and the matrix renders the Eshelby conjecture invalid; i.e. the clast values are no longer constant, as displayed in the non-end member cases of Figs. 2 and 3. Qualitatively, the lubricant allows propagation of the outside pressure perturbations into the lubricant and the clast. In the case of the maximum shear stress the lubricant represents a ring of low values, which cause lower values in the outer parts of the strong clast as previously observed by Kenkmann (2000). The influence of a lubricant layer may essentially be summarized as follows. The less viscous (Fig. 2b and c, e and f)

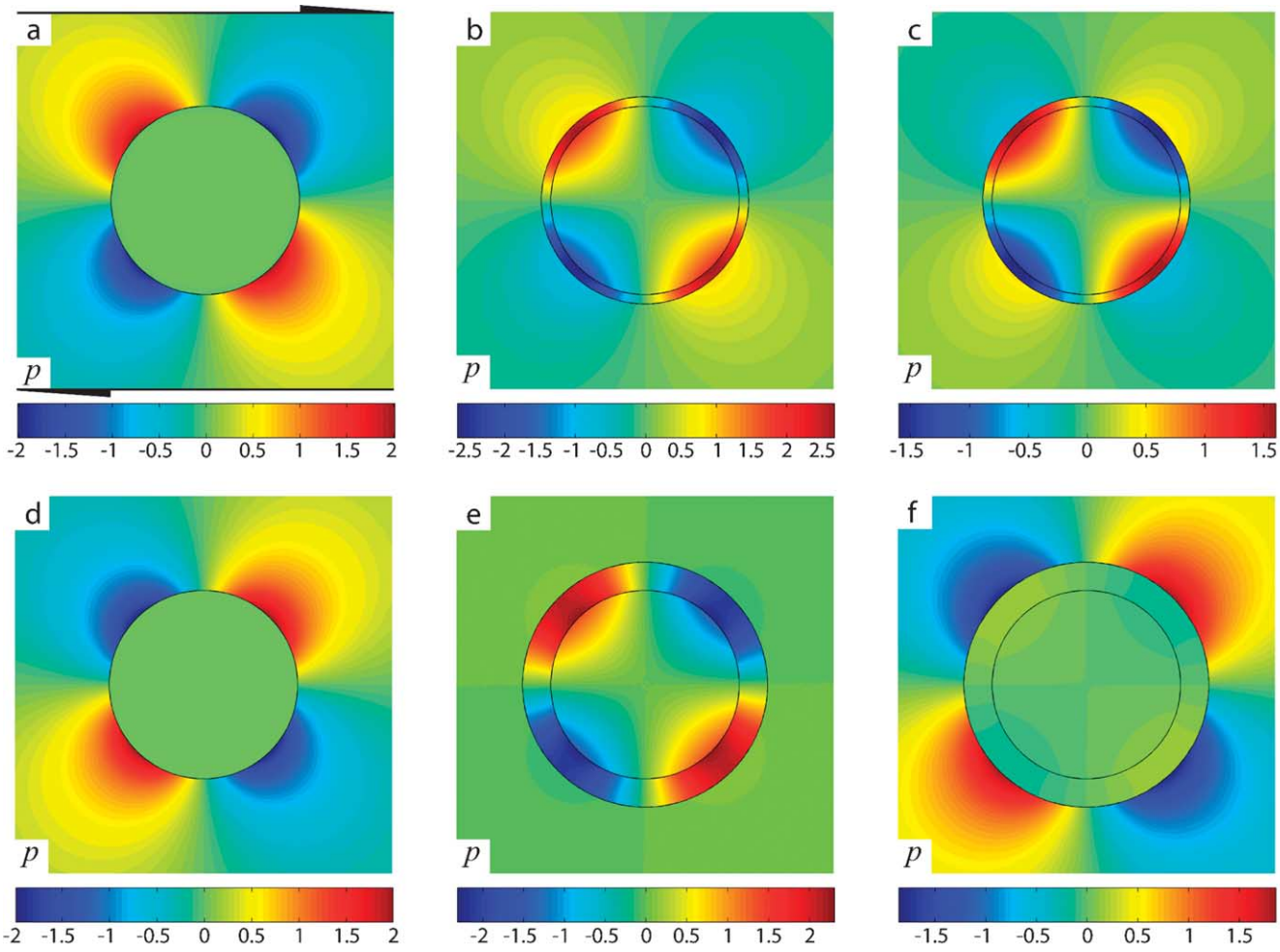

Fig. 2. Pressure perturbations caused by circular inclusions with rims of varying thickness and viscosity in simple shear. Note that (i) the shear sense in all experiments is top to the right, (ii) only the region immediately surrounding the inclusion is displayed but the full model is much larger, and (iii) all viscosities are normalized by η_{matrix} (as is always the case throughout this paper). (a) $H=0$, $\eta_{clast}=1000$; (b) $H=10$, $\eta_{clast}=1000$, $\eta_{lubricant}=1/10$; (c) $H=10$, $\eta_{clast}=1000$, $\eta_{lubricant}=1/1000$; (d) $H=0$, $\eta_{clast}=1/1000$; (e) $H=30$, $\eta_{clast}=1000$, $\eta_{lubricant}=1/10$; (f) $H=30$, $\eta_{clast}=1000$, $\eta_{lubricant}=1/1000$.

or the thicker the lubricant layer is relative to the clast (Fig. 2b and e, c and f), the more the pressure perturbation field in the matrix and inside the clast–lubricant couple starts to resemble the case of the weak inclusion directly bonded to the matrix; compare Fig. 2f with Fig. 2d. The same holds for the maximum shear stress; compare Fig. 3f with Fig. 3d.

3.2. Effect of finite strain

The effect of large strain is illustrated in Fig. 4, based on the rigid circular inclusion with $H=10$, $\eta_{lubricant}/\eta_{matrix}=1/1000$ (cf. Figs. 2c and 3c). The achieved shear strain is $\gamma=0.56$ (see Fig. 1 for the definition of γ). This is sufficient to significantly decrease the lubricant thickness in the compressive quadrants and start to form tails. The geometry of the clast–lubricant couple is ϕ-type (Passchier and Trouw, 1996), which would evolve into a σ-type with increasing strain (Ceriani et al., 2003). The stress distribution still closely resembles the corresponding initial situation, but the increasingly sharp tail tips start acting as stress concentrators, like the tips of a crack (Jaeger and Cook, 1979). Interestingly, the rotation rate $\dot{\psi}$ of the circular clast is almost unaffected by the presence of a lubricating layer. Throughout the experiment the rotation rate was essentially half the applied simple shear rate, which is the predicted value for a rigid circle perfectly bonded to the matrix (Jeffery, 1922). This observation agrees with analogue experiments (Ceriani et al., 2003) and was analytically predicted for perfect cylindrical geometries by Schmid and Podladchikov (2003).

4. Elliptical Inclusion

4.1. Initial stages—Newtonian

The characteristic behavior of lubricated elliptical inclusions is discussed based on an elliptical clast with aspect ratio 2:1 (Fig. 5). If there is no lubricant the pressure perturbation field and the maximum shear stress resemble

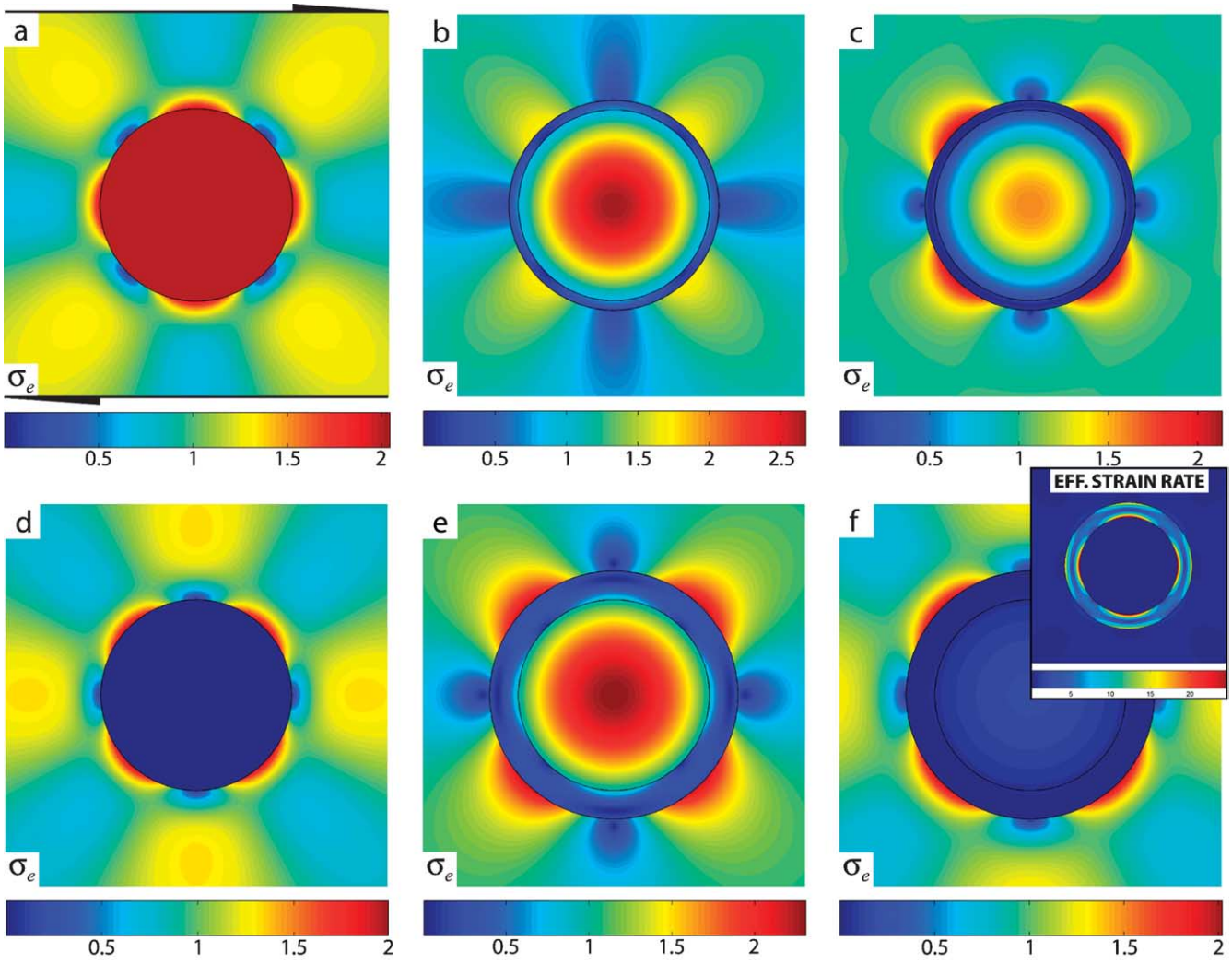

Fig. 3. Effective shear stresses caused by circular inclusions with rims of varying thickness and viscosity in simple shear. The configuration of (a)–(f) is identical to Fig. 2a–f. The insert in (f) shows the corresponding effective strain rate field.

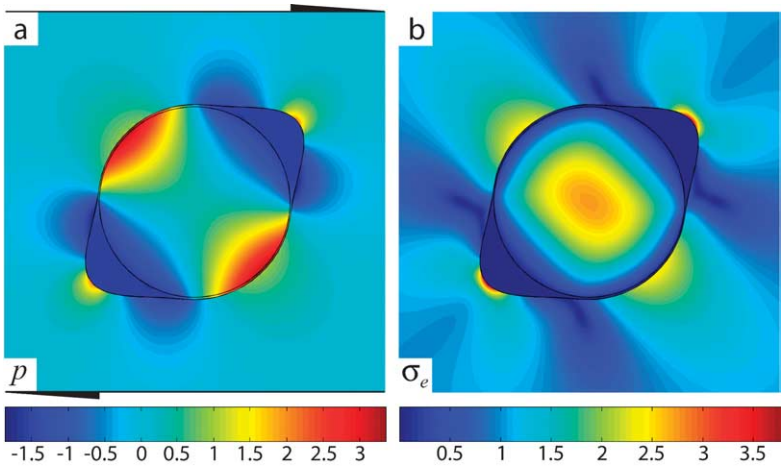

Fig. 4. Pressure perturbation (a) and effective shear stress field (b) resulting from a finite strain experiment, $\gamma = 0.56$, based on the initial configuration shown in Figs. 2c and 3c ($H = 10$, $\eta_{clast} = 1000$, $\eta_{lubricant} = 1/1000$).

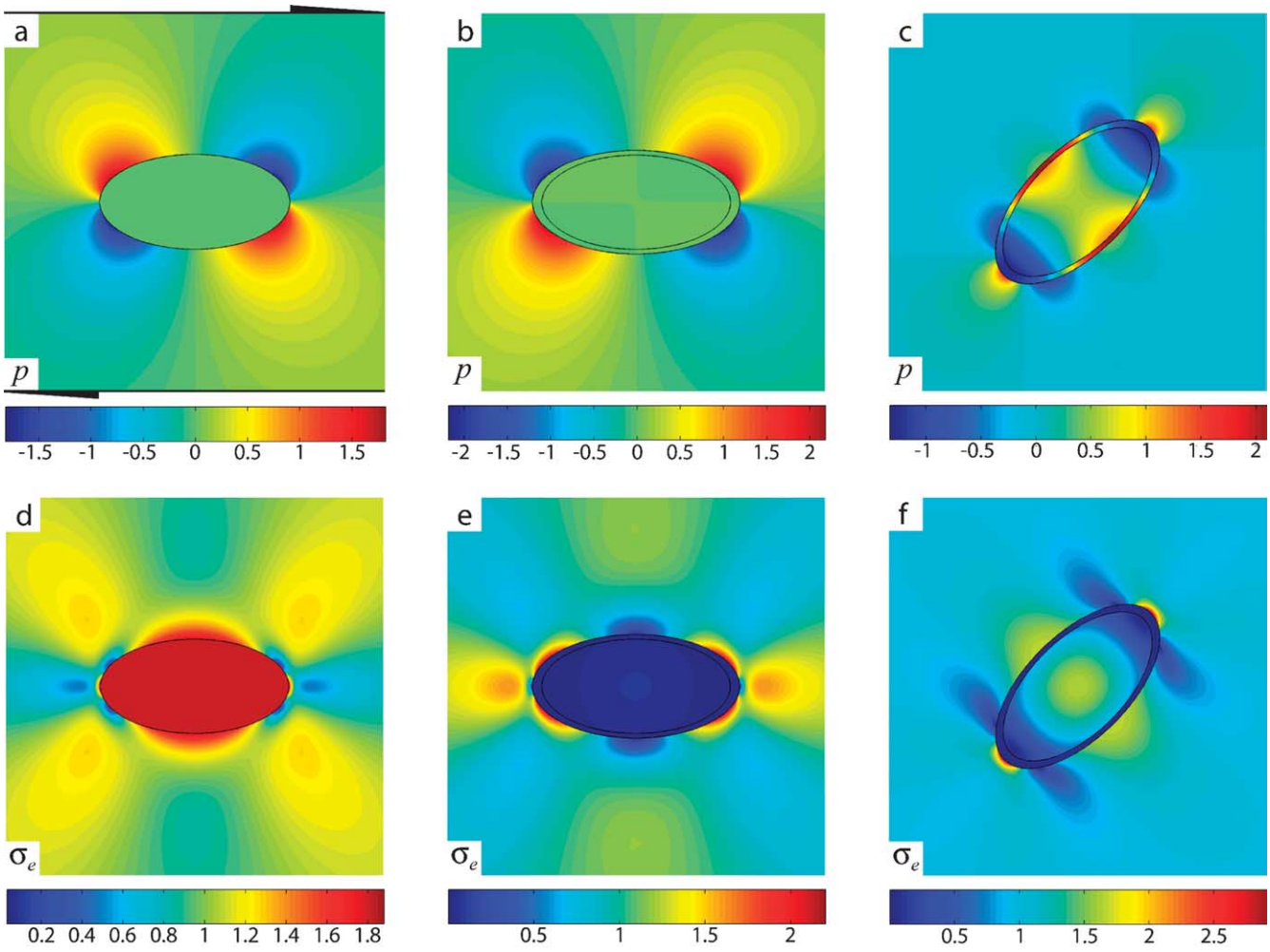

Fig. 5. Pressure perturbation ((a)–(c)) and corresponding effective shear stress fields ((d)–(f)) resulting from elliptical clasts ($a/b=2$) in simple shear. (a) and (d) $\psi=0$, $H=0$, $\eta_{clast}=1000$; (b) and (e) $\psi=0$, $H=10$, $\eta_{clast}=1000$, $\eta_{lubricant}=1/1000$; (c) and (f) $\psi=45$, $H=10$, $\eta_{clast}=1000$, $\eta_{lubricant}=1/1000$.

largely the corresponding circular case; compare Fig. 5a and d with Figs. 2a and 3a. When a lubricant is introduced in the case of a shear plane parallel elliptical clast ($\psi=0°$), a viscosity contrast of $\eta_{lubricant}/\eta_{matrix}=1/1000$ and a thickness of $H=10$ are already sufficient for the pressure perturbation and effective shear stress to vanish within the inclusion (Fig. 5b). This reflects the analytical prediction of Stagni (1991) who found that an elliptical inclusion with imperfect bonding to the matrix should remain stress free when subjected to remote simple shear parallel to the long axis of the ellipse, i.e. in this special case the Eshelby conjecture essentially holds for imperfect bonding. This can also be observed in the orthogonal case ($\psi=90°$), which is a degenerate case of the shear plane parallel ellipse. The influence of intermediate inclination angles is illustrated with the case of $\psi=45°$ in Fig. 5c and f. Interestingly, the central parts of the strong clast experience overpressure, although the clast is orientated here parallel to the direction of maximum extension of the simple shear flow.

4.2. Initial stages—power-law

Realistic rock rheologies exhibit non-linear relationships between stress and strain rate, cf. Eqs. (2) and (3). In the experiment displayed in Fig. 6 the matrix and the lubricant have a power-law exponent of three, while the clast is Newtonian with a viscosity that is a 1000 times higher than the far-field matrix value. Based on the far-field simple shear rate the effective viscosity contrast between lubricant and matrix was tailored to be 1:10. However, due to the local variations in stress and strain rate the effective viscosity contrast deviates from the predicted value. Fig. 6c and d illustrates the complexity of the non-linear material behavior by focusing on different ranges of the effective viscosity values. Where the material experiences the highest stress it exhibits the highest strain rates and consequently the effective viscosity is lowest and vice versa, cf. Fig. 6b and c. While the matrix values of effective viscosity near the clast are relatively close to the background-based predicted value of one, the values in the lubricant show larger deviations. In fact the effective viscosities in the lubricant

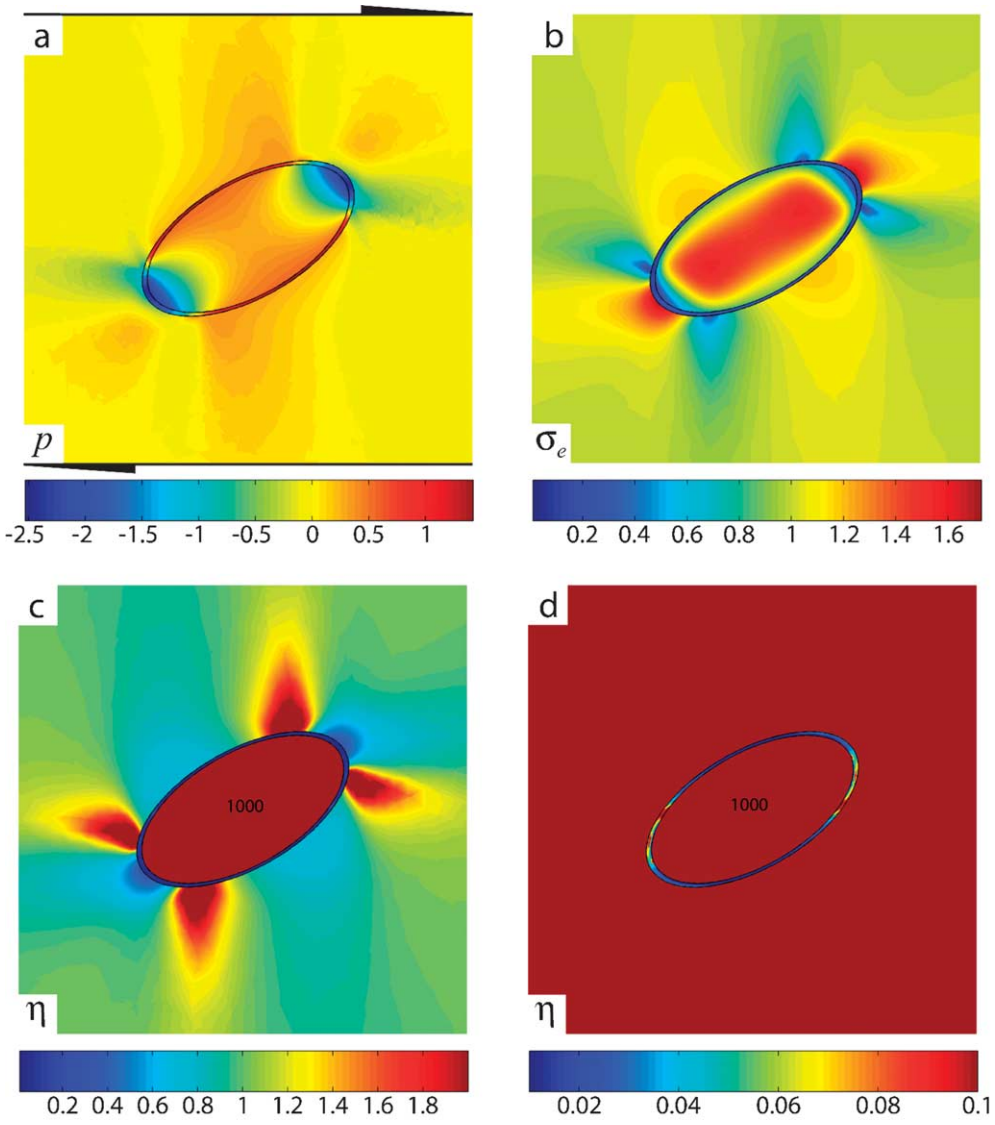

Fig. 6. Effect of non-linear power-law material properties on the pressure perturbation (a) and effective shear stress field (b) for a lubricated clast with $a/b=2$, $H=5$, and $\psi=30$. While the clast has a Newtonian viscosity of 1000, the matrix and the lubricant have a power-law exponent of three. The background strain rate ($\dot{\gamma}$) based determination of the effective viscosity contrast is $\eta_{\text{lubricant}}/\eta_{\text{matrix}}=1/10$. However, due to the deviation of the effective strain rate with respect to $\dot{\gamma}$ the actual effective viscosity contrast is larger ((c) and (d)).

are approximately one order of magnitude too low (Fig. 6d), close to 0.01 in most of the lubricant instead of the predicted 0.1. The reason is the high effective strain rate in the lubricant layer (cf. Fig. 3f). The resulting heterogeneities in the effective viscosities cause pressure and maximum shear stress fields in the model to deviate from the corresponding Newtonian case. However, some of the basic characteristics in terms of high and low locations and patterns of dynamic parameters such as pressure and maximum shear stress are preserved.

4.3. Finite strain

The finite strain behavior of lubricated elliptical clasts is illustrated in Fig. 7, based on the previously discussed experiment in Fig. 5b and e ($a/b=2$, $H=10$, and $\eta_{\text{lubricant}}/\eta_{\text{matrix}}=1/1000$). The achieved shear strain in Fig. 7 is $\gamma=0.86$, which suffices to substantially decrease the lubricant thickness in the compressive quadrants, to form σ-type tails, and bring the particle into a meta-stable position. As in the case of the circular inclusion the progressively increasing sharpness of the tail tips acts as a stress concentrator.

In contrast to the circular case the introduction of a lubricant layer has a drastic effect on the rotational behavior of the elliptical inclusion (cf. Fig. 8). Starting from its initial position parallel to the shear flow the clast rotates backwards, i.e. antithetically against the applied simple shear flow. With increasing shear strain the inclusion approaches a quasi-stable inclination of approximately 30° to the shear plane. This inclination is not truly stable due to

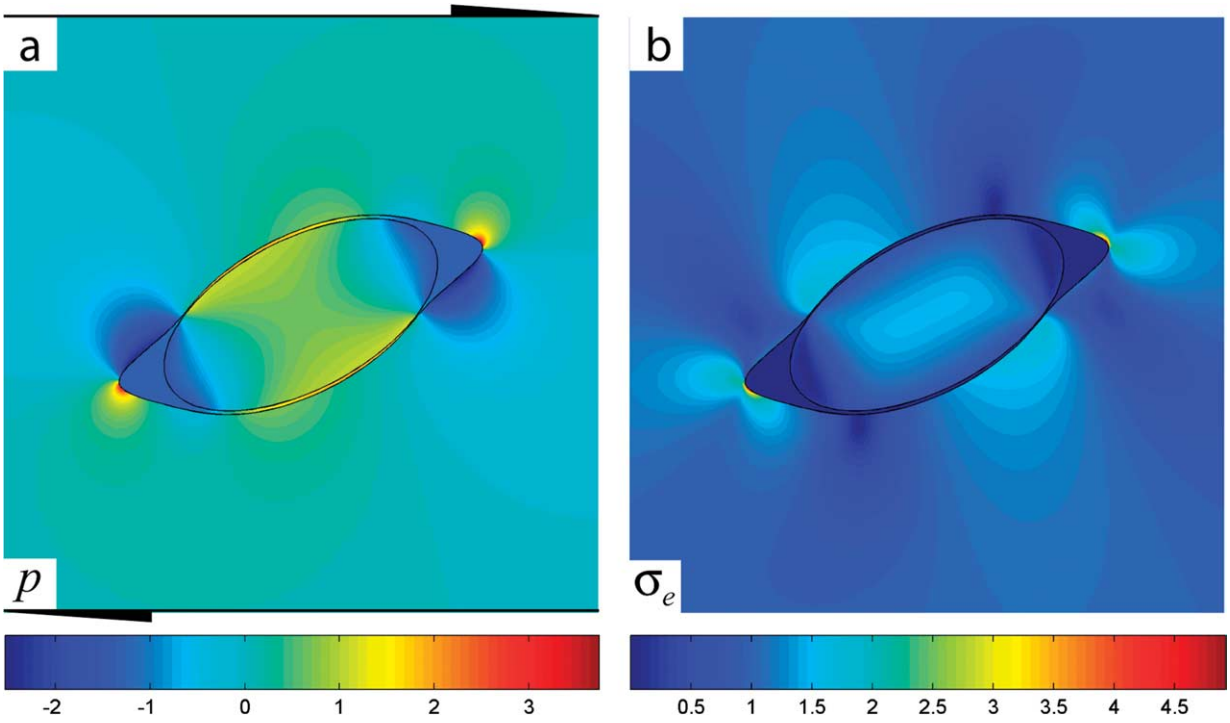

Fig. 7. Finite strain experiment. From its initially shear-plane parallel orientation the clast–lubricant couple rotates antithetically against the applied shear and develops a σ-type shape. $a/b=2$, $H=10$, $\eta_{\text{clast}}=1000$, $\eta_{\text{lubricant}}=1/1000$, $\gamma=0.86$.

the continuous movement of lubricant towards the tails. With decreasing lubricant thickness the particle is expected to resume its synthetic (forward) rotation, move towards the shear plane, and eventually rotate again according to Jeffery's theory (Ceriani et al., 2003).

5. Lubricated inclusion rotation map (LIRM)

5.1. Construction concept

The effect of a lubricant layer can be summarized as follows The introduction of a lubricant substantially alters the dynamics (p and σ_e) and the kinematics ($\dot{\psi}$) of elliptical inclusions. On the other hand, the progressive development of tails does not appear to significantly influence the dynamics or the kinematic behavior of the inclusion, which was also demonstrated by means of analogue modeling (Ceriani et al., 2003). The tails act in a crack-like manner far away from the strong clast, yet the stress distribution in the direct vicinity of the inclusion remains almost identical to the case of a lubricated porphyroclast without tails. Therefore the influence of the tails is purely one of mass balance: the formation of tails reduces the thickness of lubricant

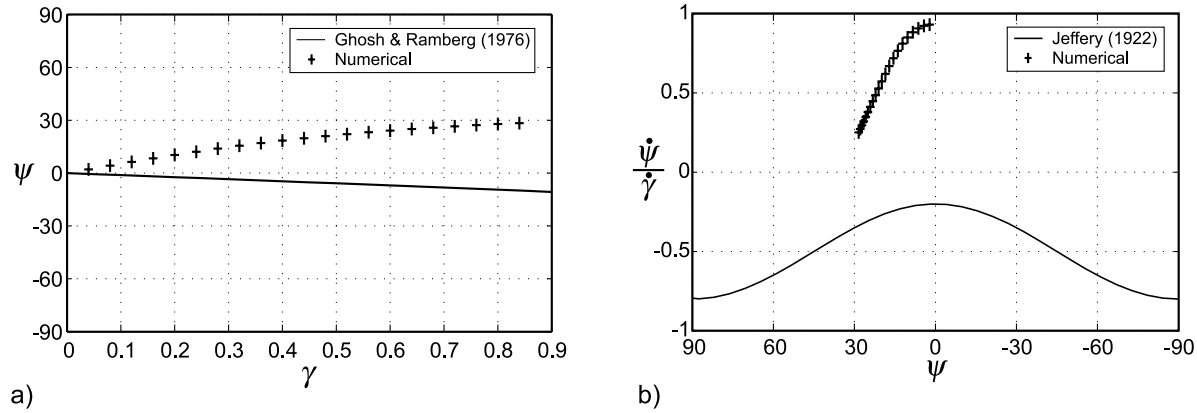

Fig. 8. Analysis of the finite strain experiment from Fig. 7. (a) Shows the evolution of inclination with increasing shear strain and makes the comparison with the Ghosh and Ramberg (1976) theory. (b) Plots the normalized rotation rate versus the inclination resulting from the numerical experiment and from Jeffery's (1922) analytical theory. Note that both analytical theories were derived for perfect bonding between clast and matrix and are plotted here to illustrate the drastic effect that a lubricating layer (or imperfect bonding) has on the clast behavior.

material around the inclusion. We deduce that tail formation is not a first order effect and we test this hypothesis by comparing instantaneous, single time-step experiments with finite strain experiments. This is done with the aid of a so-called 'lubricated inclusion rotation map' (LIRM). Each LIRM summarizes several hundred single time step experiments in which, for a given aspect ratio and lubricant viscosity, the rotation rate $\dot{\psi}$ and the lubricant thickness change rate $\dot{H}$ were measured as a function of orientation angle ψ and lubricant thickness H (at the intersection of the clast ellipse short axis with the lubricant layer). Note that all rates are normalized by the far-field simple shear rate $\dot{\gamma}$, i.e. for small time Δt intervals these rates are:

$$\dot{\psi} = \frac{1}{\dot{\gamma}} \frac{\Delta\psi}{\Delta t} \tag{6}$$

$$\dot{H} = \frac{1}{\dot{\gamma}} \frac{\Delta H}{\Delta t} = \frac{1}{\dot{\gamma}} \frac{\Delta h}{b\Delta t} 100 \tag{7}$$

$\dot{H}$ is a key parameter because it characterizes the lubricant behavior over the largest part of the inclusion surface, i.e. the sides sub-parallel to the long axis. $\dot{H}$ controls whether this channel-like region increases or decreases in thickness, in competition with the tails. In contrast to the tails, these lubricant channels exert tractions on the clast and therefore must be considered when studying the behavior of an elongated, lubricated inclusion. Indeed, the comparison with a channel flow driven by pressure gradients seems appropriate if the pressure along the channel is taken into account. It is clear from the figures in the previous section that pressures are highest near the center of the channel and lowest in the pressure shadow zones into which the material is expelled.

The two building blocks of a LIRM, $\dot{H}$ and $\dot{\psi}$ as a function of ψ and H, are shown in Fig. 9a and b, with the example of an inclusion of aspect ratio 2:1 and lubricant to matrix viscosity contrast of 1/1000 (linear viscous). As already demonstrated the introduction of a lubricant layer has a strong influence on the rotation rates (Fig. 9b). With increasing H, the rotation rates go rapidly from Jeffery's solution (zero lubricant) into a steady field in which back-rotation occurs for orientations close to the shear-plane. For the present case of large viscosity contrast between matrix and lubricant, this steady field is reached with only 2% lubricant. The $\dot{\psi}$ field is always symmetric around $\psi = 0$. $\dot{H}$, on the other hand, does not show this symmetry around $\psi = 0$, is more sensitive to the amount of lubricant, and does not show a steady state with respect to H (Fig. 9a).

For lubricated clasts at any location in the $\psi - H$ plane $\dot{\psi}$ and $\dot{H}$ essentially represent velocity vectors, which describe where in the plane the clast will move to next. $\dot{\psi}$ represents the vertical velocity component and is characterized by the back-rotation field around $\psi = 0$ (underlain in dark gray; Fig. 9d), which is limited by the $\dot{\psi} = 0$ contour. Once the clast has reached this contour it will stop rotating. However, for two reasons the $\dot{\psi} = 0$ contour is only meta-stable. (1) The velocity arrows in Fig. 9c point away from the negative leg of $\dot{\psi} = 0$. Hence, small perturbations will cause the clast to move away from the negative leg towards the positive leg, which, due to the vertical periodicity of the graph, can be reached from the entire $\psi - H$ plane, either by synthetic forward-rotation or antithetic back-rotation. Therefore the positive leg of $\dot{\psi} = 0$ is called 'attractor line'. (2) With respect to the clast rotation only, the attractor line is stable. However, any location in the $\psi - H$ plane is only truly stable if $\dot{\psi}$ and $\dot{H}$ vanish. Hence the velocity vector components resulting from $\dot{H}$ must also be analyzed (Fig. 9c). Analogous to $\dot{\psi}$ the bulk behavior can be divided into two regions. Inside the $\dot{H} = 0$ contour (underlain in light gray) the lubricant thickness at the ellipse short axes decreases, outside it increases. Since neither the contours of $\dot{\psi} = 0$ and $\dot{H} = 0$ in this, nor in any other experiment performed, intersect in the positive half of the $\psi - H$ plane the attractor lines must also be considered meta-stable (unless mantle material production rate is considered, which is done below).

$\dot{\psi}$ and $\dot{H}$ are the building blocks of a LIRM. If we add the individual velocity vector components we obtain total velocity vectors in the $\psi - H$ plane (Fig. 9e). These velocity vectors should approximate the complex finite strain behavior of mantled clasts. In order to verify this, finite strain experiments like the one in Fig. 7 were performed with randomly chosen starting positions in the $\psi - H$ plane and their trace plotted as solid arrows on the presented LIRM (aspect ratio, viscosity contrasts, and power-law exponents, $n = 1$, were kept identical in the single time step and finite strain experiments). The traces of the finite strain experiments follow the velocities derived from single time step experiments quite well and clearly indicate the attraction potential of the attractor line. This substantiates the hypothesis that the tails are not a key parameter in the mantled porphyroclast system and the complex finite strain behavior of mantled clasts can be approximated by single time step experiments with perfect elliptical geometries.

5.2. Influence of viscosity contrast and production of mantle material

In order to account for the natural variability in aspect ratios and viscosity contrasts, LIRMs and the corresponding attractor lines must be calculated for every individual case If, for the given aspect ratio of 2/1, the viscosity contrast between lubricant and matrix is increased from 1/1000 to 1/50,000 essentially the same result (attractor line) is obtained. However, decreasing the viscosity contrast from 1/1000 to 1/2 (Fig. 9f) leads to the observation that (i) the corresponding maximum inclination angle of the attractor line decreases, (ii) the field of back-rotation therefore becomes smaller, and (iii) more lubricant (larger H) is required for stopping the clast rotation. In the case of a

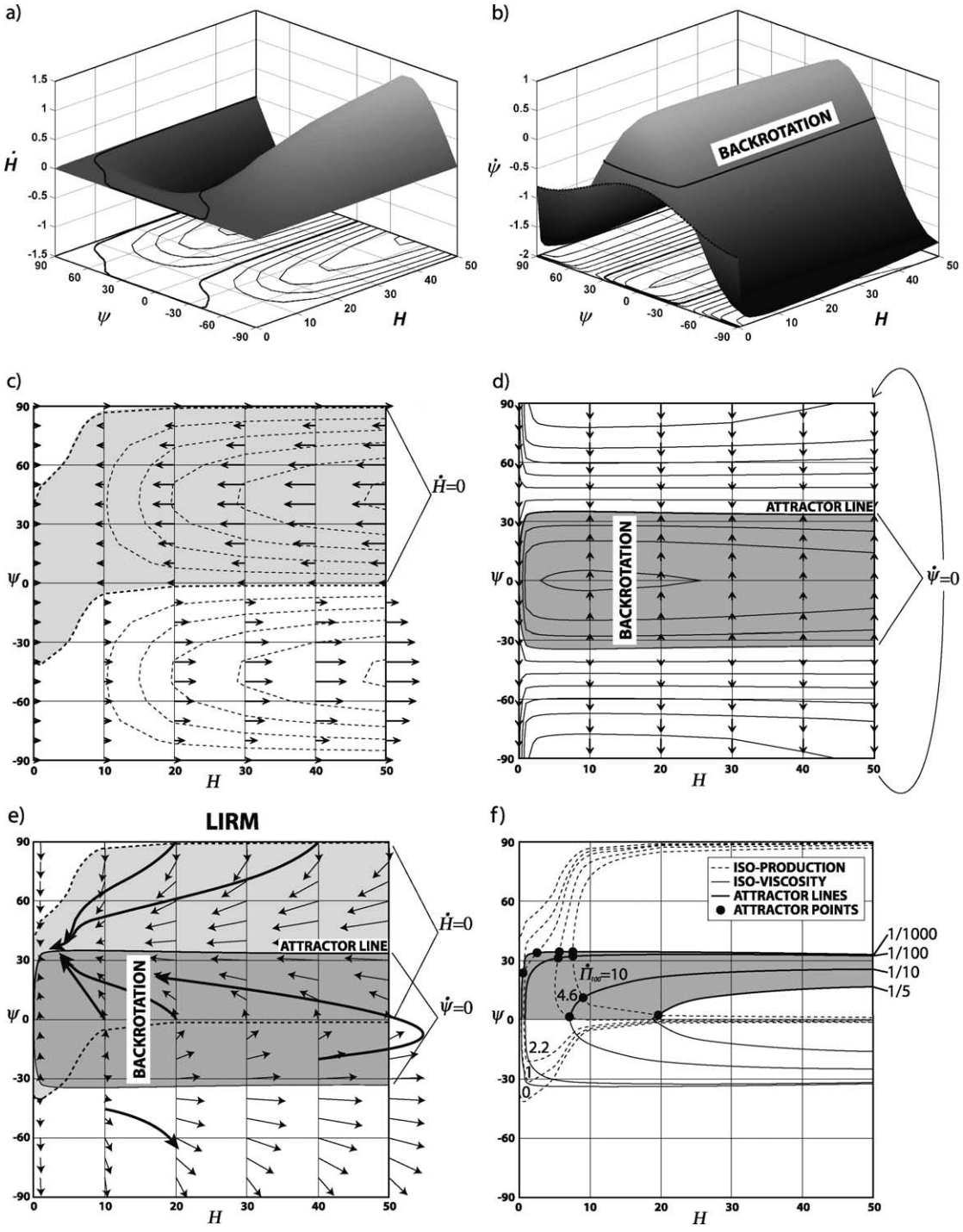

Fig. 9. Construction of a 'lubricated inclusion rotation map' (LIRM) illustrated by means of a Newtonian example with $a/b = 2$, $\eta_{clast} = 1000$, $\eta_{lubricant} = 1/1000$. For each position in the $\psi - H$ plane a single time step experiment is performed and the rotation rate ($\dot{\psi}$) and the lubricant thickness change rate at the ellipse short axis ($\dot{H}$) measured. (a) Instantaneous lubricant thickness change rate as a function of inclination and lubricant thickness. (b) Instantaneous rotation rate as a function of inclination and lubricant thickness. (c) Velocity vectors resulting from the thickness change rate only. (d) Velocity vectors resulting from the rotation rate only. Note the vertical periodicity and the attractor line (see text). (e) LIRM with the total velocity vectors resulting from the single time step experiments (thin, short arrows) and the $\psi - H$ plane traces of finite strain experiments (thick, long arrows). (f) Influence of lubricant viscosity on the attractor lines (solid lines), and mantle production rate on the zero thickness change rate contours (dashed lines). Since the attractor lines and the total $\dot{H} = 0$ contour now intersect in the upper half of the graph depending on the mantle production rate, truly stable attractor points come into existence. Note that for better readability the values of the mantle production rate are multiplied by a hundred, symbolized by $\dot{\Pi}_{100}$, and the $\eta_{lubricant}/\eta_{matrix}$ values are given at the right side of the plot.

viscosity contrast between lubricant and matrix of only 1/2 the lubrication was not sufficient to cause back-rotation.

Another key parameter is the production rate of mantle material. LIRMs are constructed with a given amount of lubricant surrounding the strong clast. However, in natural mylonites the lubricant mantle is expected to develop progressively during ongoing deformation. With the onset of deformation, local stress concentrations around the porphyroclast could lead to local cataclasis (e.g. Tullis and Yund, 1987), crystal–plastic re-crystallization, or formation of new phases. In this context it is important to note the difference in scaling between velocities and stresses. While, for given shear strain rate, the absolute values of the velocities around the clast decrease with decreasing size of the clast; this is not the case for the amplitudes of the local stresses. It is clear from dimensional and analytical arguments (Jaeger and Cook, 1979; Schmid and Podladchikov, 2003) that the stresses are independent of clast size and do not decrease with decreasing clast size, opposite to what was proposed by Passchier and Simpson (1986).

As an approximation we assume that the lubricant is derived from the clast and produced all around the elliptical clast with a production rate $\dot{\Pi}$, which is defined analogous to $\dot{H}$, cf. Eq. (7). $\dot{\Pi}$ describes the change in the thickness solely due to the conversion of clast material into mantle. The total change in lubricant thickness is now the sum of $\dot{\Pi} + \dot{H}$ and therefore the zero contour lines of the (total) thickness change rate in Fig. 9c are altered (cf. Fig. 9f). Depending on the values, intersection points between the attractor lines ($\dot{\psi} = 0$) and the zero mantle thickness change rate (total $\dot{H} = 0$) exist now for positive inclinations and non-zero lubricant thicknesses. Once such a point is reached a clast will remain at the corresponding inclination as long as the lubricant thickness, i.e. $\dot{\Pi}$, remains constant. Since these intersection points are truly stable they are termed 'attractor points'. Attractor points can only exist inside the field (underlain in gray; Fig. 9f) bounded by the attractor line where the system loses sensitivity to further increases in the viscosity contrast between lubricant and matrix (1/1000) and the minimum viscosity contrast attractor line where back-rotation still occurs (1/5).

6. Attractor maps

The existence of attractor points can be summarized with 'attractor maps'. For a given clast aspect ratio and power-law exponent configuration all possible attractor points are calculated and the corresponding lubricant to matrix viscosity contrast and mantle production values contoured (Fig. 10). Attractor maps are a potentially useful tool because the three simple geometrical parameters, clast inclination ψ, mantle thickness H, and clast aspect ratio, allow for direct estimation of mantle production rate $\dot{\Pi}$ and the viscosity contrast between mantle and matrix. The attractor maps also allow for a comprehensive overview over the size of the fields in which stable inclinations occur (underlain in gray in Fig. 10), the maximum possible inclination angle, and where back-rotation is to be expected. The characteristics of the attractor maps are:

1. The iso-viscous attractor lines show the same tendency for all aspect ratios and rheologies, namely that decreasing the viscosity of the lubricant (relative to the matrix) widens the field of back-rotation in the $\psi - H$ plane.
2. Once the viscosity of the lubricant is smaller than 1/1000 of the matrix value, the behavior of the inclusion is no more sensitive to a further decrease in lubricant viscosity.
3. Increasing the aspect ratio leads to a decrease in the maximum stable inclination angle.
4. For all Newtonian rheologies ($n = 1$), the lubricant viscosity has to be less than 1/2 of the matrix value for back-rotation to occur.
5. The introduction of a power-law lubricant allows stabilization to occur for an already effective viscosity contrast of 1/2, which is, however, largely due to the underestimation of the actual effective viscosity contrast.
6. The introduction of power-law rheology outside the clast increases the maximum stable inclination angle.
7. Despite the differences between the corresponding power-law and Newtonian attractor maps, the main characteristics are identical and therefore the Newtonian maps may be used for a first parameter estimation.

7. Application of attractor map method

7.1. Viscosity contrast and mantle production rate estimation

The primary use of the presented attractor maps is to estimate the rate at which the clast material was turned into mantle material and for approximating the effective viscosity contrast between mantle and matrix The required data are simple geometrical parameters, measurable in the field or thin sections. This procedure is demonstrated with the example of the mica fish in Fig. 11. The mica is embedded in a quartz rich matrix, the shear sense is top to the left, and the shear plane is horizontal. Relative to the shear plane, the clast shows a positive inclination, which is assumed to be stable. The clast is surrounded by finer grained material that is derived from the clast and long but very thin tails exist.

The geometrical parameters needed for the attractor map method are aspect ratio, inclination, and mantle thickness. The first two parameters are easily determined and the values are $a/b = 3.5$ and $\psi = 14°$. The attractor map that comes closest to the measured aspect ratio was generated for $a/b = 3$, and we assume applicability of the Newtonian

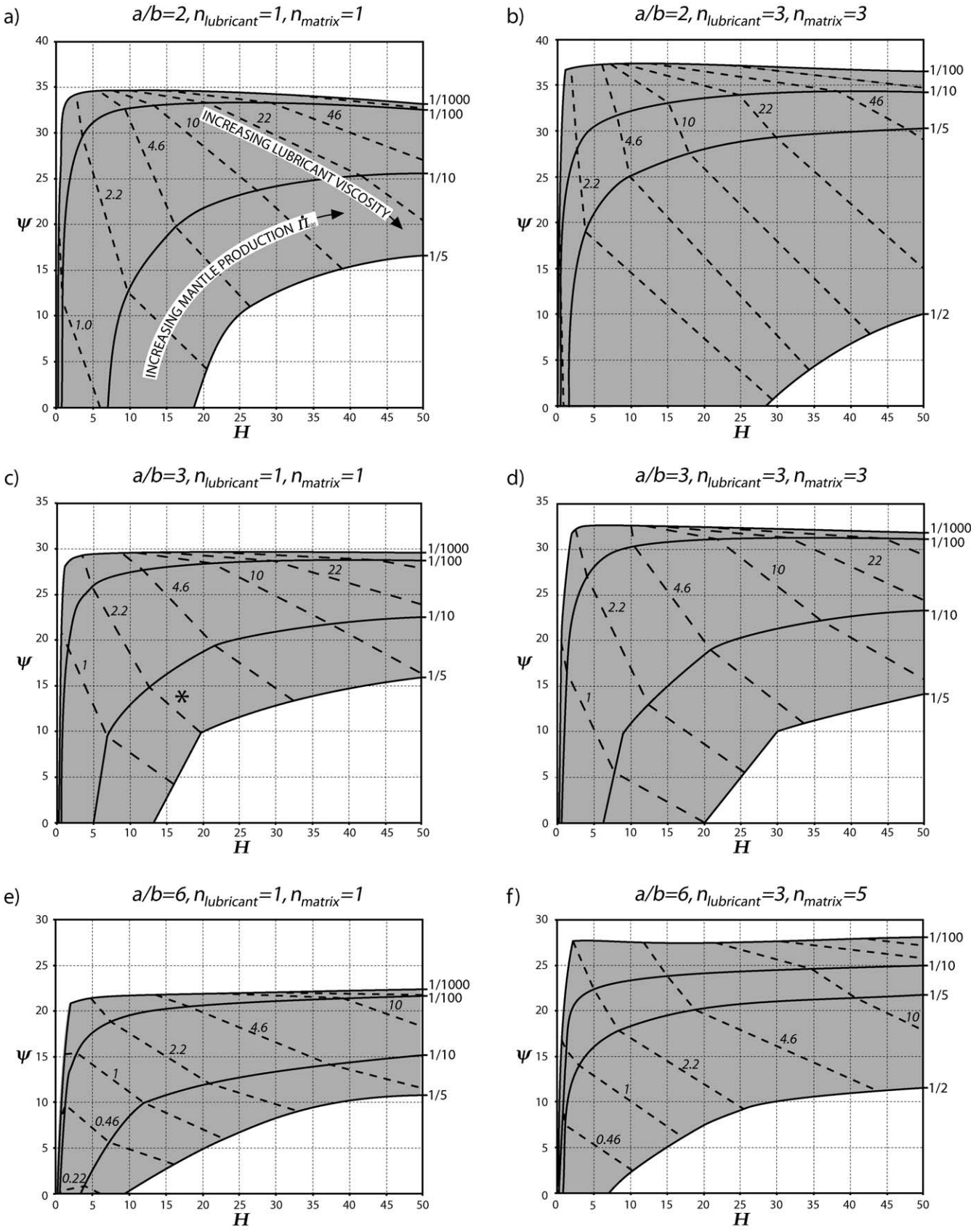

Fig. 10. Attractor maps. Attractor maps allow for viscosity contrast and mantle production rate estimation if three simple, directly measurable geometrical parameters are known: a/b, H, and ψ. Rows show attractor maps with identical aspect ratio, columns compare Newtonian (first) to power-law cases (second).

version (Fig. 10c). Since the clast is not perfectly elliptical, several ways exist to determine H, as shown in the insert of Fig. 11. However, the average value is around $H \approx 17$, and it is obvious from the corresponding attractor map (Fig. 10c) that H variations in the observed range are not significant. The measured values of ψ and H are represented by the star in Fig. 10c. Interpolation yields estimates of mantle material production rate and viscosity contrast between matrix and mantle material. This reveals that the viscosity contrast between the matrix and the mantle was rather small, in the range of 1/5–1/10, and the mantle material production rate is approximately $\dot{I}\dot{I} \approx 0.025$. Thus, if the position of the mica is indeed stable, it needs to produce 0.025% mantle material (relative to b) per $\Delta\gamma = 1$ to maintain the present inclination. Both obtained parameters, the effective mantle–matrix viscosity contrast and the mantle material production rate, are in a reasonable range that could be expected for natural mylonites.

7.2. Shear strain estimation

The attractor map method has been derived as a tool for estimating the rate at which mantle material is produced and the viscosity contrast between matrix and mantle. However, if it is possible to determine the total area of mantle material, M, we can use the obtained estimate of $\dot{I}\dot{I}$ to estimate the total amount of shear strain. The corresponding equation is:

$$\gamma = 100\frac{M}{cb\dot{I}\dot{I}} \tag{10}$$

where c is the circumference of the elliptical clast. The natural clast example shown in Fig. 11 has very long and narrow tails that are almost impossible to identify and indicate a large amount of shear strain. Calculating based on the clearly visible mantle material and evaluating Eq. (10) yields a shear strain estimate of $\gamma \approx 320$. This is a rather large value. However, over the 60 μm height of the picture in Fig. 11 such a shear strain corresponds to differential horizontal displacement of less than 2 cm.

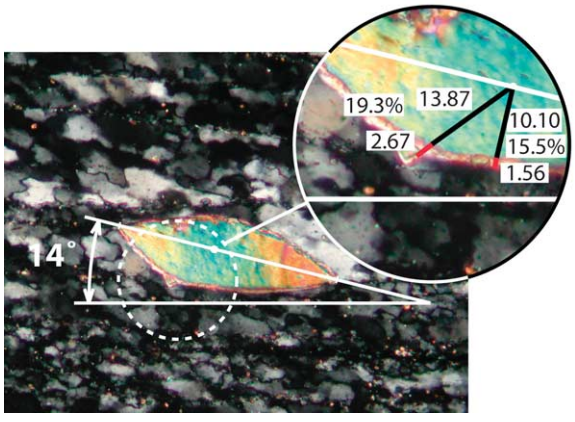

Fig. 11. Example of attractor map method application. 60-μm-high picture of a mica fish from the Dent Blanche nappe. The shear sense in this picture-parallel shear zone is top to left. Measured aspect ratio is $a/b = 3$, inclination $\psi = 14°$, and mantle thickness is $H \approx 17$. Photo courtesy G. Pennacchioni.

Cases like the one shown in Fig. 11 where the area of the mantle material cannot be determined may still yield shear strain estimates. Assuming that the mantle material is derived from the clast, knowledge of the original clast size can be utilized to calculate γ. In nature, statistics of clast sizes inside and outside shear zones may be used to approximate the amount of mantle material produced. Or it may simply be assumed that the largest clast size outside the shear zone corresponds to the largest clast size within the shear zone. More generally, the method may be applicable to poly-phase rocks that show a distinct orientation and grain size when subjected to shear. These hypotheses should and could be tested either by laboratory experiments with torsion rigs, with field examples, or direct numerical simulations.

8. Limitations of the attractor map method

In order to be able to tackle the complexity of the mantled porphyroclast system we have made a number of assumptions. Nevertheless, more than 8000 experiments were necessary to infer the characteristic behavior of this simplified system. Some of the major limitations of the attractor map method are discussed in the following.

Clasts in natural mylonites can have complex forms that substantially deviate from the elliptical shapes assumed. However, it has been shown by Ferguson (1979) and Arbaret et al. (2001) for the classical Jeffery solution that even if strongly non-elliptical objects are used, the ellipse shape-based theory remains an excellent approximation of the rotational behavior. Concerning the validity of the presented attractor maps we expect to see a similar insensitivity to actual clast shape. Indeed, Mancktelow et al. (2002) have shown that lubricated rhomboidal particles show the same characteristic back-rotational and stable inclination behavior as observed here.

Another limitation that should be considered is that in nature clasts with systematic orientation are observed but they do not have a visible mantle. Given the small mantle material production rates required to stabilize clasts, the lack of mantle surrounding the clast may be just apparent. In cases where there is indeed no mantle present it may be likely that such clasts have imperfect bonding to the matrix (Samanta and Bhattacharyya, 2003), which may be considered as the limiting case of a lubricant layer, where the thickness goes to zero, normal tractions are continuous, but shear tractions vanish. Therefore the clast behavior will effectively follow the descriptions above. Yet, the attractor maps will not be applicable since there is no actual lubricant layer that is perfectly bonded to the clast and the matrix.

Previous explanations of systematic clast stabilization have frequently been based on the combined effect of pure and simple shear. This paper focuses only on simple shear

and ignores possible pure shear components. If an additional pure shear component is present the results may be altered; however, mylonites are characterized by large amounts of shear accumulated in relatively narrow zones and consequently simple shear dominates the system. Under these conditions, the combined pure and simple shear theory does not exhibit stable inclinations and can be ruled out (Schmid and Podladchikov, 2004).

Care has been taken to avoid boundary or clast interaction effects. This simplifies the analysis but is to some extent unrealistic since the clast densities in mylonites may lead to clast interaction. It has been shown by Ildefonse et al. (1992) that the interaction effects become significant if individual clasts are closer than one diameter, and this distance is assumed to be the limit of applicability of the presented work. In addition, shear zone boundaries may affect the behavior of natural clasts as pointed out by Marques and Coelho (2001) and Taborda et al. (2004).

Another important aspect is that natural shear zones accommodate large amounts of strain through strain partitioning whereby large areas do not deform much and most strain is concentrated in the narrow zones that make up the so-called C–S fabrics (Berthe et al., 1979; Lister and Snoke, 1984). If a C–S fabric is present, local shear flows may differ from the bulk shear and consequently the shear strain recorded by a clast may not be representative for the bulk of the rock mass (ten Grotenhuis et al., 2002).

9. Conclusions

We have investigated the mantled porphyroclast in a shear zone as a true three-phase system where the viscosity of the mantle material is lower than the matrix and the strong clast. We have shown that the introduction of a weak mantle has a dominant influence on the distribution and amplitudes of effective strain rates, pressures, and maximum shear stresses. The most prominent effects related to the presence of a weak mantle are found in the clast kinematics, where we demonstrated that for a large set of parameters the clast has meta-stable positions that are always at positive inclinations relative to the shear plane and direction (attractor lines). In order to reach these positions the clast can either rotate with the applied shear or against it, depending on the starting position. If the mantle material production rate is accounted for, then stable inclination angles may result. These inclination angles range from 0 to 40°, depending on the viscosity contrast between matrix and mantle, the power-law exponent of the materials, the thickness of the mantle, the mantle material production rate, and the aspect ratio. Generally, the stable inclination angle decreases with growing aspect ratio, which is in agreement with observations of clasts in natural shear zones (ten Grotenhuis et al., 2002).

Systematic investigation of the behavior of the lubricated clast in a shear zone results in attractor maps. These maps are a novel tool for estimating the mantle material production rate and the viscosity contrast between mantle and matrix by means of simple geometrical parameters. In combination with the area of the clast and the mantle, the knowledge of the mantle material productivity rate yields an approximation for the total shear strain. In the absence of conventional shear strain markers, such as vein offsets, this new method can provide estimates for the shear strain.

Acknowledgements

This research was supported by the ETH Zurich, grant TH 0-20650-99. We wish to thank Jean-Pierre Burg, Stefano Ceriani, Neil Mancktelow, Fernando Ornelas and Karel Schulmann for helpful and inspiring discussions. The review by Paul Bons and the editorial comments by Tom Blenkinsop are gratefully acknowledged.

References

Arbaret, L., Mancktelow, N.S., Burg, J.P., 2001. Effect of shape and orientation on rigid particle rotation and matrix deformation in simple shear flow. Journal of Structural Geology 23, 113–125.

Berthe, D., Choukroune, P., Jegouzo, P., 1979. Orthogneiss, mylonite and non coaxial deformation of granites—example of the South-Armorican-Shear-Zone. Journal of Structural Geology 1, 31–42.

Bons, P.D., Barr, T.D., ten Brink, C.E., 1997. The development of delta-clasts in non-linear viscous materials: a numerical approach. Tectonophysics 270, 29–41.

Brezzi, F., Fortin, M., 1991. Mixed and Hybrid Finite Elements Methods. Springer-Verlag, New York.

Ceriani, S., Mancktelow, N.S., Pennacchioni, G., 2003. Analogue modelling of the influence of shape and particle/matrix interface lubrication on the rotational behaviour of rigid particles in simple shear. Journal of Structural Geology 25, 2005–2021.

Crouzeix, M., Raviart, P.A., 1973. Conforming and nonconforming finite-element methods for solving stationary stokes equations. Revue Francaise D Automatique Informatique Recherche Operationnelle 7, 33–75.

Eshelby, J.D., 1959. The elastic field outside an ellipsoidal inclusion. Proceedings of the Royal Society of London Series A—Mathematical and Physical Sciences 252, 561–569.

Ferguson, C.C., 1979. Rotations of elongate rigid particles in slow non-Newtonian flows. Tectonophysics 60, 247–262.

Furuhashi, R., Huang, J.H., Mura, T., 1992. Sliding inclusions and inhomogeneities with frictional interfaces. Journal of Applied Mechanics—Transactions of the Asme 59, 783–788.

Gao, Z., 1995. A circular inclusion with imperfect interface: Eshelby's tensor and related problems. Journal of Applied Mechanics—Transactions of the Asme 62, 860–866.

Ghosh, S.K., Ramberg, H., 1976. Reorientation of inclusions by combination of pure shear and simple shear. Tectonophysics 34, 1–70.

ten Grotenhuis, S.M., Passchier, C.W., Bons, P.D., 2002. The influence of strain localisation on the rotation behaviour of rigid objects in experimental shear zones. Journal of Structural Geology 24, 485–499.

Hanmer, S., Passchier, C.W., 1991. Shear sense indicators: a review. Geological Survey of Canada 90, 1–71.

Ildefonse, B., Sokoutis, D., Mancktelow, N.S., 1992. Mechanical

interactions between rigid particles in a deforming ductile matrix—analog experiments in simple shear-flow. Journal of Structural Geology 14, 1253–1266.

Jaeger, J.C., Cook, N.G.W., 1979. Fundamentals of Rock Mechanics. Chapman and Hall, London.

Jeffery, G.B., 1922. The motion of ellipsoidal particles immersed in a viscous fluid. Proceedings of the Royal Society of London A102, 161–179.

Kenkmann, T., 2000. Processes controlling the shrinkage of porphyroclasts in gabbroic shear zones. Journal of Structural Geology 22, 471–487.

Lister, G.S., Snoke, A.W., 1984. S–C mylonites. Journal of Structural Geology 6, 617–638.

Mancktelow, N.S., Arbaret, L., Pennacchioni, G., 2002. Experimental observations on the effect of interface slip on rotation and stabilisation of rigid particles in simple shear and a comparison with natural mylonites. Journal of Structural Geology 24, 567–585.

Marques, F.O., Coelho, S., 2001. Rotation of rigid elliptical cylinders in viscous simple shear flow: analogue experiments. Journal of Structural Geology 23, 609–617.

Mura, T., 1987. Micromechanics of Defects in Solids. Nijhoff, Dordrecht.

Mura, T., 2000. Some new problems in the micromechanics. Materials Science and Engineering A (Structural Materials: Properties Microstructure and Processing) 285, 224–228.

Muskhelishvili, N.I., 1953. Some Basic Problems of the Mathematical Theory of Elasticity. Noordhoff, Groningen.

Passchier, C.W., Simpson, C., 1986. Porphyroclast systems as kinematic indicators. Journal of Structural Geology 8, 831–843.

Passchier, C.W., Trouw, R.A.J., 1996. Microtectonics. Springer, Berlin.

Passchier, C.W., Tenbrink, C.E., Bons, P.D., Sokoutis, D., 1993. Delta-objects as a gauge for stress sensitivity of strain-rate in mylonites. Earth and Planetary Science Letters 120, 239–245.

Pennacchioni, G., Fasolo, L., Cecchi, M.M., Salasnich, L., 2000. Finite-element modelling of simple shear flow in Newtonian and non-Newtonian fluids around a circular rigid particle. Journal of Structural Geology 22, 683–692.

Pennacchioni, G., Di Toro, G., Mancktelow, N.S., 2001. Strain-insensitive preferred orientation of porphyroclasts in Mont Mary mylonites. Journal of Structural Geology 23, 1281–1298.

Piazolo, S., Passchier, C.W., 2002. Experimental modeling of viscous inclusions in a circular high-strain shear rig: implications for the interpretation of shape fabrics and deformed enclaves. Journal of Geophysical Research–Solid Earth 107 (BIO), 2242, doi:10.1029/2000JB000030.

Piazolo, S., Bons, P.D., Passchier, C.W., 2002. The influence of matrix rheology and vorticity on fabric development of populations of rigid objects during plane strain deformation. Tectonophysics 351, 315–329.

Ranalli, G., 1995. Rheology of the Earth. Chapman and Hall, London.

Ru, C.Q., Schiavone, P., 1997. A circular inclusion with circumferentially inhomogeneous interface in antiplane shear. Proceedings of the Royal Society of London Series A—Mathematical Physical and Engineering Sciences 453, 2551–2572.

Samanta, S.K., Bhattacharyya, G., 2003. Modes of detachment at the inclusion–matrix interface. Journal of Structural Geology 25, 1107–1120.

Schmid, D.W., Podladchikov, Y.Y., 2003. Analytical solutions for deformable elliptical inclusions in general shear. Geophysical Journal International 155, 269–288.

Schmid, D.W., Podladchikov, Y.Y., 2004. Are isolated stable rigid clasts in shear zones equivalent to voids? Tectonophysics 384, 233–242.

Shen, H., Schiavone, P., Ru, C.Q., Mioduchowski, A., 2001. Stress analysis of an elliptic inclusion with imperfect interface in plane elasticity. Journal of Elasticity 62, 25–46.

Simpson, C., Wintsch, R.P., 1989. Evidence for deformation-induced K-feldspar replacement by myrmekite. Journal of Metamorphic Geology 7, 261–275.

Stagni, L., 1991. Elastic field perturbation by an elliptic inhomogeneity with a sliding interface. Journal of Applied Mathematics and Physics 42, 811–820.

Taborda, R., Antunes, J., Marques, F.O., 2004. 2-D rotation behavior of a rigid ellipse in confined viscous simple shear: numerical experiments using FEM. Tectonophysics 379, 127–137.

Ten, A.A., Yuen, D.A., 1999. Time-dependent formation of mantled inclusion structures for different rheologies under a simple shear. Earth and Planetary Science Letters 165, 25–35.

Tullis, J., Yund, R.A., 1987. Transition from cataclastic flow to dislocation creep of feldspar—mechanisms and microstructures. Geology 15, 606–609.